NASA Technical Memorandum 104039

SPATIAL ADAPTION PROCEDURES ON UNSTRUCTURED MESHES FOR ACCURATE UNSTEADY AERODYNAMIC FLOW COMPUTATION

RUSS D. RAUSCH
JOHN T. BATINA
HENRY T. Y. YANG

MARCH 1991

National Aeronautics and Space Administration

Langley Research Center
Hampton, Virginia 23665

SPATIAL ADAPTION PROCEDURES ON UNSTRUCTURED MESHES FOR ACCURATE UNSTEADY AERODYNAMIC FLOW COMPUTATION

Russ D. Rausch*
Purdue University
West Lafayette, Indiana 47907

John T. Batina†
Unsteady Aerodynamics Branch
Structural Dynamics Division
NASA Langley Research Center
Hampton, Virginia 23665–5225

Henry T. Y. Yang‡
Purdue University
West Lafayette, Indiana 47907

Abstract

Spatial adaption procedures for the accurate and efficient solution of steady and unsteady inviscid flow problems are described. The adaption procedures were developed and implemented within a two-dimensional unstructured-grid upwind-type Euler code. These procedures involve mesh enrichment and mesh coarsening to either add points in high gradient regions of the flow or remove points where they are not needed, respectively, to produce solutions of high spatial accuracy at minimal computational cost. The paper gives a detailed description of the enrichment and coarsening procedures and presents comparisons with alternative results and experimental data to provide an assessment of the accuracy and efficiency of the capability. Steady and unsteady transonic results, obtained using spatial adaption for the NACA 0012 airfoil, are shown to be of high spatial accuracy, primarily in that the shock waves are very sharply captured. The results were obtained with a computational savings of a factor of approximately fifty-three for a steady case and as much as twenty-five for the unsteady cases.

Introduction

Considerable progress has been made over the past decade in developing methods of dynamically-adapting computational meshes based on the numerical solution of partial differential equations.[1] These methods are being developed to produce higher spatial accuracy in such solutions more efficiently. Spatial accuracy is obviously important when modelling continuous equations with a discrete set of points. It is generally understood, of course, that accuracy is improved when the number of mesh points in a fixed computational domain is increased. Associated with an increase in the number of mesh points, however, are increased computer run times and memory costs, which are proportional to the number of mesh points. Hence, for efficiency, it is important to enrich meshes *locally* based on the numerical solution, in contrast to using *globally* fine meshes, to minimize the total number of mesh points and hence minimize the cost for a given spatial accuracy. The methods of mesh adaption can be separated into three general categories: (1) mesh regeneration, (2) mesh movement, and (3) mesh enrichment. The first method, mesh regeneration, places the work of adapting the mesh on the mesh generation program rather than on the actual numerical solution procedure of the governing equations. In this method, a solution is first obtained, and regions of relatively large discretization errors are detected. A new mesh is then generated to concentrate points in regions where the large discretization errors occur. This new mesh may contain more or fewer points than the original mesh. For the second method, mesh movement, the number of points in the computational domain remains fixed. To resolve more accurately the solution spatially, these points are moved into regions where solution gradients are relatively large. In general, this can be accomplished by two different ways. The first way models the mesh as a spring network, where points are joined by linear springs with spring stiffnesses proportional to solution gradients. The mesh is then allowed to move into the relatively high gradient regions to produce effectively a locally finer mesh. The second way uses forcing functions in a Poisson-equation grid generator to redistribute points. Either method of mesh movement is easily implemented within existing solution algorithms because only the locations of the existing mesh points are changed. The final method of spatial adaption is mesh enrichment. In this method points are added to regions of relatively large so-

*Graduate Research Assistant, School of Aeronautics and Astronautics, Member AIAA.

†Senior Research Scientist, Unsteady Aerodynamics Branch, Structural Dynamics Division, Senior Member AIAA.

‡Professor and Dean, Schools of Engineering, Fellow AIAA.

lution error by dividing locally the cells which make up the mesh or by embedding finer meshes in these regions. This method differs from mesh regeneration and movement in that the mesh is made finer in local regions while the global mesh topology remains the same. The method of mesh enrichment is also generally regarded as having advantages over regeneration and movement, especially for transient problems, because of the higher degree of flexibility in being able to add points where they are needed and to remove points where they are not needed. The disadvantage, however, is that the implementation of mesh enrichment involves significant modification to existing solution algorithms.

For the Euler and Navier-Stokes equations, computational fluid dynamics algorithms are being developed based on spatial adaption methods. With these equations, relatively large spatial discretization errors may be encountered with flow features such as shock waves, shear layers, boundary layers, and expansion fans. These flow features can be resolved more accurately using the adaption methods mentioned above. Nakahashi et al,[2] for example, has used tension and torsional springs to move the mesh into regions where relatively large spatial discretization errors occur. This mesh movement approach showed considerable versatility for the problems treated. However, various constants were needed to control orthogonality and smoothness, and direct control of an optimal mesh adaption procedure was generally not possible. Further examples of spatial adaption methods include the work of Usab and Murman.[3] In Ref. 3, embedded meshes of quadrilateral cells and nodes were used in regions of the mesh where shock waves occurred. This approach improved the spatial accuracy of the numerical method which resulted in highly accurate solutions for steady flow problems. Dannenhoffer and Baron[4,5] extended the work in this area using irregularly shaped embedded regions, which were coupled to the base mesh by a multiple-grid solution algorithm. Several other examples of spatial adaption include methods which use flow solvers based on unstructured triangular and tetrahedral meshes in two and three dimensions, respectively. Peraire et al.[6,7] used mesh regeneration coupled with a finite element solution algorithm to sharply capture shock waves and complex shock structures. Lohner et al.[8-13] have developed a procedure to locally enrich the mesh for transient flow problems by dividing elements which make up a base mesh to capture shock waves. Further, in this procedure, elements may be removed (coarsened) from the mesh if they are not necessary to produce a given level of spatial accuracy.

With respect to solution algorithms based on unstructured meshes, the results published by the authors[14] demonstrated that these algorithms produce steady and unsteady solutions of comparable accuracy to results obtained using structured-grid solution algorithms. The two sets of results presented in Ref. 14 were obtained using meshes of comparable density, and mesh adaption was not used. Solutions of higher spatial accuracy are indeed possible through the use of mesh adaption. Therefore, the purpose of this paper is to report on modifications to the two-dimensional unstructured-grid upwind-type Euler code of Batina[15] to include mesh enrichment and coarsening procedures. The objectives of the research are as follows: (1) to develop time-accurate enrichment and coarsening procedures for spatial adaption, (2) to test the procedures by performing steady and unsteady calculations for a variety of cases, (3) to determine the accuracy of the spatially adapted solutions by making comparisons with published solutions produced by alternative methods and existing experimental data and (4) to assess the efficiency of the spatially adapted solutions by making comparisons of required computer resources. The eventual goal is to develop a highly accurate and efficient solution algorithm for the Euler and Navier-Stokes equations for aeroelastic analysis of complex aircraft configurations. The paper gives a detailed description of the mesh enrichment and coarsening procedures and gives a brief description of the solution algorithm of Ref. 15 for completeness. Steady and unsteady transonic results are presented for the NACA 0012 airfoil to demonstrate applications of the spatial adaption procedures. The unsteady flow results for the NACA 0012 airfoil were obtained for the airfoil pitching harmonically about the quarter chord.

Upwind-Type Euler Solution Algorithm

The unsteady Euler equations are solved using the two-dimensional upwind-type solution algorithm developed by Batina.[15] The solution algorithm, which is a cell-centered finite-volume scheme,[15-17] uses upwind differencing based on flux-vector splitting similar to upwind schemes developed for use on structured meshes. The present unstructured grid algorithm is thus referred to as an upwind-type solution algorithm. The spatial discretization of this algorithm involves a so-called flux-split approach based on the flux-vector splitting of van Leer.[18] The flux-split discretization accounts for the local wave-propagation characteristics of the flow and captures shock waves sharply with at most one grid point within the shock structure. A further advantage is that the discretization is naturally dissipative and consequently does not require additional artificial dissipation terms or the adjustment of free parameters to control the dissipation. However, in calculations involving higher-order upwind schemes, oscillations in the solution near shock waves are expected to occur. To eliminate these oscillations, flux limiting is usually required. In the present study, a continuously differentiable flux limiter was employed.[15-17]

The Euler equations are integrated in time using an implicit time-integration scheme involving a Gauss-Seidel relaxation procedure.[15] The relaxation procedure is implemented by reordering the elements that make up the unstructured mesh from upstream to downstream. The solution is obtained by sweeping two times through the mesh as dictated by stability considerations. The first sweep is performed in

the direction from upstream to downstream and the second sweep is from downstream to upstream. For purely supersonic flows the second sweep is unnecessary. This relaxation scheme is stable for large time steps and allows the selection of the step size based on the temporal accuracy required for the problem being considered, rather than on the numerical stability of the algorithm. Consequently, very large time steps may be used for rapid convergence to steady state and an appropriate step size may be selected based on temporal convergence for unsteady cases, independent of numerical stability issues.

Weighted Averaging

A weighted averaging procedure is used in the two-dimensional upwind-type Euler solution algorithm to interpolate the cell-centered values of the primitive variables to the nodes. As illustrated in Fig. 1, the weighted average of the cell-centered values q_i surrounding a node is given by,

$$q_0 = \frac{\sum_{i=1}^{n} w_i q_i}{\sum_{i=1}^{n} w_i} \tag{1}$$

where the nodal value q_0 is computed using the cell weights w_i. Several different weights have been used in this procedure including the areas of surrounding cells and the reciprocal distance from the node to the locations of cell centers. Because of the disparity in cell sizes that occur when using spatial adaption, the most accurate weighted averaging is desired. Therefore, a different approach for computing the weights has been developed based on the work of Holmes and Connell.[19] In Ref. 19, artificial dissipation for a node-based Navier-Stokes solution algorithm was computed using a Laplacian operator. The Laplacian $L(\phi_0)$ at a node was computed by

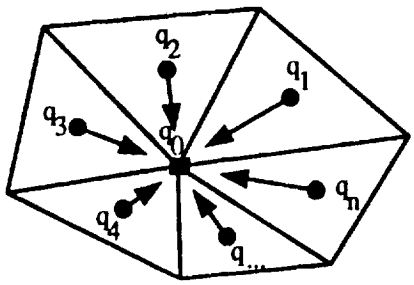

Fig. 1 Difference star for computing the weighted average q_0 of surrounding cell-centered values $q_{1\cdots n}$.

$$L(\phi_0) = \sum_{i=1}^{n} w_i(\phi_i - \phi_0) \tag{2}$$

using the surrounding nodal values ϕ_i and the weights w_i. The weights were derived by first noting that the Laplacian of a linear function is exactly zero. Since this is a desirable property to require of the computed Laplacian, the weights w_i in Eq. (2) were derived with this objective. Therefore, the spatial locations (x_i, y_i) of ϕ_i were substituted into Eq. (2) resulting in

$$L(x_0) = \sum_{i=1}^{n} w_i(x_i - x_0) = 0 \tag{3}$$

$$L(y_0) = \sum_{i=1}^{n} w_i(y_i - y_0) = 0 \tag{4}$$

The weights were then determined by defining

$$w_i = 1 + \Delta w_i \tag{5}$$

where

$$C = \sum_{i=1}^{n} (\Delta w_i)^2 \tag{6}$$

is a cost function. The cost function C was minimized to keep the weights close to unity by solving an optimization problem given the constraints of Eqs. (3) and (4). The optimization problem was solved using the method of Lagrange multipliers where Δw_i was given by

$$\Delta w_i = \lambda_x(x_i - x_0) + \lambda_y(y_i - y_0) \tag{7}$$

The solution yielded Lagrange multipliers, defined by

$$\lambda_x = \frac{(I_{xy}R_y - I_{yy}R_x)}{(I_{xx}I_{yy} - I_{xy}^2)} \tag{8}$$

$$\lambda_y = \frac{(I_{xy}R_x - I_{xx}R_y)}{(I_{xx}I_{yy} - I_{xy}^2)} \tag{9}$$

where

$$R_x = \sum_{i=1}^{n} (x_i - x_0) \tag{10}$$

$$R_y = \sum_{i=1}^{n} (y_i - y_0) \tag{11}$$

$$I_{xx} = \sum_{i=1}^{n} (x_i - x_0)^2 \tag{12}$$

$$I_{yy} = \sum_{i=1}^{n} (y_i - y_0)^2 \tag{13}$$

$$I_{xy} = \sum_{i=1}^{n} (x_i - x_0)(y_i - y_0) \tag{14}$$

Note that the weights were computed solely from the distance between node locations and no special treatment was required near mesh boundaries.

Modifications were made to this procedure for computing the Laplacian in order to develop a new procedure for computing the weights in Eq. (1). The first modification was to express the Laplacian at the nodes using surrounding cell-centered values, as illustrated in Fig. 1, rather than the surrounding nodal values. Now the Laplacian at the node can be expressed by

$$L(q_0) = \sum_{i=1}^{n} w_i(q_i - q_0) \tag{15}$$

where q_0 represents the unknown value at the node and q_i are the known values at the surrounding cell-centers. The weights w_i in Eq. (15) are now computed using the node location (x_0, y_0) and the surrounding cell-center locations (x_i, y_i). Recalling that the computed Laplacian for a linear function is zero, then for a linear variation of q

$$\sum_{i=1}^{n} w_i(q_i - q_0) = 0 \tag{16}$$

which can be rewritten in the form given by Eq. (1). Therefore, using the weights from the Laplacian procedure, Eq. (1) is an exact interpolation of the nodal value q_0 for a linear variation of cell-centered values q_i. For a nonlinear variation of cell-centered values q_i, the weighted averaging procedure using the weights from the Laplacian procedure is second order accurate in space. Although the procedure is computationally more expensive than area or reciprocal distance weighted averaging, the increased cost is relatively small compared to the cost of solving the Euler equations.

Spatial Adaption Procedures

In this section, the spatial adaption procedures are described in detail. These descriptions include explanations of the flow feature detection and the procedures used to enrich and coarsen the mesh.

Flow Feature Detection

The first step of the spatial adaption procedure is the detection of regions of relatively large discretization error so that the computational mesh can be locally enriched to improve the spatial accuracy or locally coarsened to reduce the computational costs. These regions generally occur near flow features such as shock waves, stagnation points, slip lines, and expansion fans for the Euler equations, where the dominant flow feature for the cases considered in this study is a shock wave.

There are a number of flow parameters that can be used for enrichment indicators based on the detection of shock waves. Parameters such as density, pressure, or total velocity are useful since these quantities are discontinuous through shocks. For example, first or second, divided or undivided differences in one of these parameters, similar to the work by Dannenhoffer and Baron,[4] can be used to detect shock waves. A specific example of an enrichment indicator is the magnitude of the density gradient $|\nabla\rho|$ which is often used to detect shock waves for steady flow problems. However, for unsteady flows, a measure of the temporal as well as the spatial variation of the solution is needed. For this reason, the absolute value of the substantial derivative of density $\left|\frac{D\rho}{Dt}\right|$ was used as an enrichment indicator, since it is the sum of the local rate of change $\frac{\partial\rho}{\partial t}$ as well as the convective rate of change $\vec{u}\cdot\nabla\rho$ of density. The substantial derivative of density can also be written as

$$\frac{D\rho}{Dt} = \frac{\partial\rho}{\partial t} + \nabla\cdot\rho\vec{u} - \rho\nabla\cdot\vec{u} \tag{17}$$

where the first two terms on the right-hand-side of Eq. (17) are simply the continuity equation. The third term can be viewed as a simplified continuity equation that assumes steady, incompressible, linear flow. Therefore, the difference between these two continuity equations results in a measure of the 1) unsteadiness, 2) compressibility, and 3) nonlinearities of the flow. Since the first two terms on the right-hand-side of Eq. (17) are zero from the continuity equation, the substantial derivative of density can be rewritten as

$$\frac{D\rho}{Dt} = -\rho\nabla\cdot\vec{u} \tag{18}$$

For unsteady flows, the substantial derivative works well for detecting developing shock waves, whereas the more commonly used enrichment indicators based on the instantaneous solution such as first or second differences in density tend to miss the initial shock wave formation. This is especially true for cases where the shock waves periodically appear and disappear in time. Other indicators, based on the substantial derivative of x-momentum ρu, y-momentum ρv, and energy e have also been investigated. These substantial derivatives are written as

$$\frac{D\rho u}{Dt} = \left\{\frac{\partial\rho u}{\partial t} + \frac{\partial(\rho u^2 + p)}{\partial x} + \frac{\rho uv}{\partial y}\right\} - \left\{\frac{\partial p}{\partial x} + \rho u\nabla\cdot\vec{u}\right\} \tag{19}$$

$$\frac{D\rho v}{Dt} = \left\{\frac{\partial\rho v}{\partial t} + \frac{\partial\rho uv}{\partial x} + \frac{\partial(\rho v^2 + p)}{\partial y}\right\} - \left\{\frac{\partial p}{\partial y} + \rho v\nabla\cdot\vec{u}\right\} \tag{20}$$

$$\frac{De}{Dt} = \left\{\frac{\partial e}{\partial t} + \frac{\partial(e+p)u}{\partial x} + \frac{\partial(e+p)v}{\partial y}\right\} - \{\nabla\cdot(\rho\vec{u}) + e\nabla\cdot\vec{u}\} \tag{21}$$

where once again each derivative results in the difference between a complete conservation equation and an approximate

equation. The first expression in brackets on the right-hand-side of Eqs. (19)-(21) is zero for the Euler x-momentum, y-momentum, and energy equations, respectively. The last expression in brackets is an approximate equation of the respective conservation laws. For example, the second equation in brackets in Eq. (19) can be derived from the conservation of x-momentum equation if the equation is simplified by assuming the local rate of change $\frac{\partial}{\partial t}$ and the convective rate of change $\vec{u} \cdot \nabla$ of x-momentum is zero. Therefore, as one might expect, if the absolute value of Eq. (19) is used as an enrichment indicator it would detect regions of the flow where the x-momentum is most rapidly changing. Similarly, Eqs. (20) and (21) would detect the rate of change of y-momentum and energy, respectively. To evaluate each expression as an enrichment indicator, the substantial derivatives of the conserved variables were computed for a transient shock problem. In this study, the performance of each of the substantial derivatives in detecting shock waves was found to be similar. It is not surprising, however, since all of the indicators involve the same term $\nabla \cdot \vec{u}$.

To detect viscous flow features, the idea of using the difference between complete equations and approximate equations can be expanded upon by considering the differences between the momentum or energy equation of the Navier-Stokes equations and an approximate inviscid equation. For example, using the momentum equation of the Navier-Stokes equations, the substantial derivative of x-momentum can be written as

$$\frac{D\rho u}{Dt} = \left\{ \frac{\partial \rho u}{\partial t} + \frac{\partial(\rho u^2 + p - \tau_{xx})}{\partial x} + \frac{\partial(\rho uv - \tau_{xy})}{\partial y} \right\} - \left\{ \frac{\partial p}{\partial x} + \rho u \nabla \cdot \vec{u} - \frac{\partial \tau_{xx}}{\partial x} - \frac{\partial \tau_{xy}}{\partial y} \right\} \tag{22}$$

This, of course, is similar to Eq. (19) except that the viscous fluxes $\left(\frac{\partial \tau_{xx}}{\partial x}, \frac{\partial \tau_{xy}}{\partial y}\right)$ have been added and subtracted on the right-hand-side. Therefore, using the ideas above, an enrichment indicator E for detecting inviscid as well as viscous flow features can be constructed by eliminating the viscous fluxes from the second expression enclosed in brackets of Eq. (22) and is written as

$$E = \left| \frac{\partial p}{\partial x} + \rho u \nabla \cdot \vec{u} \right| \tag{23}$$

Although the enrichment indicator in Eq. (23) is not used in this study, it is mentioned to demonstrate a procedure for constructing an indicator based on the governing viscous flow equations. The enrichment indicator used in this study, however, was the absolute value of the substantial derivative of density (Eq. (18)) since the Euler equations were used.

Mesh Enrichment

Generally, mesh enrichment is performed by starting with a relatively coarse mesh of cells and then subdividing these cells until a given level of spatial accuracy has been obtained. To prevent cells from being enriched too many times near flow discontinuities such as shock waves, an upper bound is placed on the number of times a cell can be divided. For transient problems the mesh enrichment procedure may be performed at each time step of the integration of the governing flow equations or it may be performed once every set number of time steps.

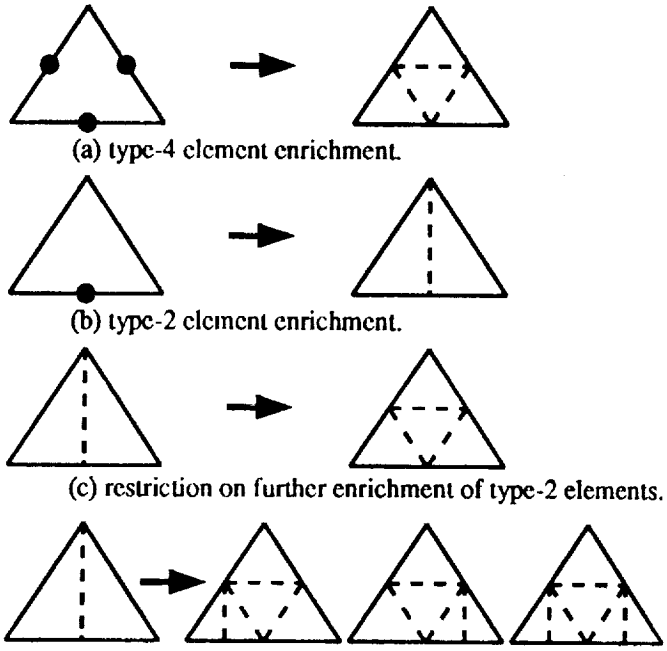

(a) type-4 element enrichment.

(b) type-2 element enrichment.

(c) restriction on further enrichment of type-2 elements.

(d) details on further enrichment of type-2 elements.

Fig. 2 Diagrams illustrating mesh enrichment possibilities.

Mesh enrichment is performed by using the enrichment indicator to determine if a cell is to be subdivided into smaller cells. To accomplish this, the enrichment indicator is computed for each cell and compared with a preset threshold value to determine whether a cell should be subdivided. If the threshold is exceeded, a new node is created at the midpoint of each edge of the triangular cell, and the cell is subdivided into four smaller cells. Special care must be taken, however, when an edge that is to be bisected lies on a boundary of the mesh, since the midpoint of the edge does not generally lie on the boundary. In this case, the location of the new node is determined by using a parametric spline of the boundary coordinates. Further, the values of the flow variables for the new cells are determined from a linear interpolation of conserved variables located at the nodes and the cell centers of the original cells.

For a given cell to be enriched, either one edge or all three edges are bisected. In the event that only two edges are marked to be bisected, the third edge is automatically bisected to prevent the creation of highly skewed or stretched cells. Each time the mesh is enriched, a cell may be divided in one of two ways, as shown in Figs. 2(a) and 2(b). The

first way, shown in Fig. 2(a), results when all three edges of a cell have been marked for enrichment. In this situation the cell is divided into four new cells where the vertices of the inner cell are in general midpoints of edges that make up the original cell. The original cell is thus referred to as a type-4 element since after enrichment it becomes four new triangular cells. The second way, shown in Fig. 2(b), occurs if only one edge of the base cell is marked for enrichment. In this situation, the marked edge is bisected, and two new cells are formed. The original cell is thus referred to as a type-2 element since after enrichment it becomes two new cells. New cells formed from a type-4 element may be enriched further. However, to prevent highly stretched cells, cells formed from a type-2 element are restricted from being divided further as indicated in Figs. 2(c) and 2(d). For cells from a type-2 element, if any of the five edges that make up the two new cells are marked for enrichment, the original cell is made into a type-4 element as shown in Fig. 2(c). If in addition to this, either or both of the bottom two edges are marked (the lower left, right, or both), cells of the type-4 element are further enriched accordingly, as shown in Fig. 2(d).

Mesh Coarsening

Generally, mesh coarsening removes added nodes and cells from previously enriched meshes to delete them from local regions of the mesh where certain flow features are no longer present. This procedure is necessary to efficiently adapt meshes to the numerical solution of the governing flow equations in order to minimize computational cost. The mesh coarsening procedure starts by marking all of the cells that do not have edges that are marked to be bisected from the mesh enrichment procedure. Figure 3 shows an example of the coarsening procedure where the dashed lines represent cells formed by a previous enrichment of the mesh. In Fig. 3(a), cells which are candidates for removal are denoted by a "1". The marked cells are then used to determine nodes that are candidates for removal. As shown in Fig. 3(b), the candidate nodes that may be removed are nodes that are surrounded by cells that are candidates for removal (identified by the "ones" in Fig. 3(a)). Cells that are to be removed from the list of candidates are determined by searching the tree data structure that stores the mesh enrichment history. Cells for removal are cells that came from type-2 or type-4 elements and are subsequently marked for removal. Once the nodes and elements have been selected they are subjected to a final simultaneous evaluation for actual removal from the mesh. Each time the mesh is coarsened, cells and nodes may be removed in one of several ways as shown in Fig. 4. (In the figure, nodes to be removed are indicated by the open circles and fixed nodes are indicated by the closed circles.) For a type-4 element, if all three of the nodes that form the inner triangle are candidate nodes, then the nodes are removed eliminating the inner triangle as shown in Fig. 4(a). This leaves only the one original cell that was previously divided into four. Similarly, if two of the three nodes that form the inner triangle are candidate nodes, the two nodes are removed and a type-2 element is formed as shown in Fig. 4(b). If only one of the candidate nodes is marked then nothing is done. For a type-2 element there is only one node that may be removed which is the midpoint of a previously bisected edge. Removal of this node leaves only the cell that was originally divided into two as shown in Fig. 4(c).

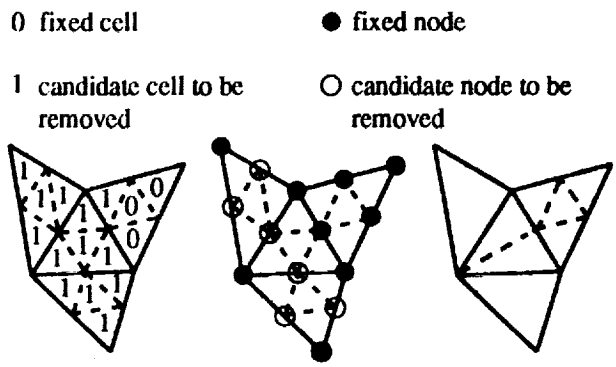

(a) identify cells to be removed. (b) identify nodes to be removed. (c) final mesh.

Fig. 3 Diagrams illustrating details of the mesh coarsening procedure.

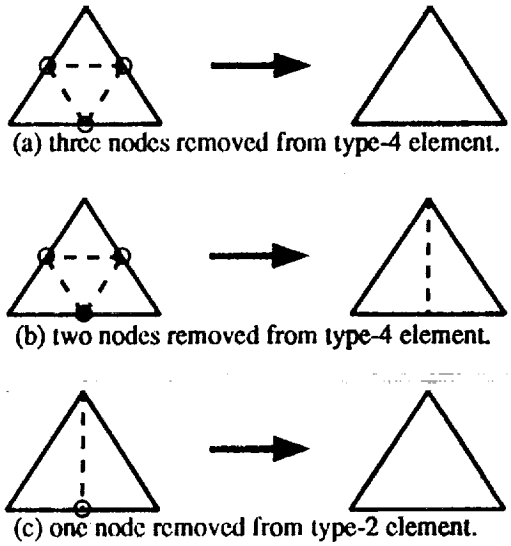

(a) three nodes removed from type-4 element.

(b) two nodes removed from type-4 element.

(c) one node removed from type-2 element.

Fig. 4 Diagrams illustrating mesh coarsening possibilities.

Temporal Convergence Considerations

Careful consideration must be given to the time-step chosen to ensure temporal convergence of unsteady problems, especially when spatial adaption procedures are used. In general the temporal convergence of the numerical solution of a time accurate problem is difficult to quantify and is related to the nondimensional time-step Δt, a characteristic length (A/s), and the local maximum characteristic wave speed $(|u| + a)$ of each cell in the computational mesh. This relation is given by the Courant-Friedrichs-Lewy (CFL) number for each cell,

$$CFL \approx \Delta t \frac{s}{A}(|u| + a) \tag{24}$$

where s is the length of a cell edge, A is the area of the cell, u is a local flow speed normal to a cell edge, and a is the local speed of sound. For unsteady problems, experience has shown that the local CFL number must remain below approximately 20 for solutions to be converged in time. However, the local allowable CFL number is highly dependent on the time-marching procedure used. For example, either explicit or implicit time-marching procedures may be used to integrate the governing flow equations in time for unsteady problems. Since the allowable CFL number based on a stability analysis of an explicit time-marching procedure is usually small compared to 20, the time-step is restricted to be relatively small. Therefore, the numerical stability of an explicit time-marching procedure dictates the time-step that can be used. For an implicit time-marching procedure, however, numerical stability of the procedure is, in general, not an issue. Hence, the time-step should be based on minimizing the effects of linearization errors, minimizing the effects of relaxation errors (or factorization errors in the case of a factored scheme), and obtaining a temporally converged solution. Irrespective of the time-marching procedure used, the spatial adaption procedures have a significant effect on the allowable time-step when the CFL number is restricted by either the temporal accuracy of the solution or the numerical stability of the solution algorithm. This effect can be demonstrated in a simple example of mesh enrichment of a single cell. Suppose, for example, the local CFL number for a cell is restricted to 20 for a temporally converged solution and the cell is enriched one level, where it is divided into four smaller cells each with area $A/4$ as shown in Fig. 5. Likewise, each edge of the cell is bisected resulting in each of the new cells having edge lengths of $s/2$. Since, from Eq. (24), the time-step is proportional to the characteristic length (A/s), the allowable time-step is halved when the cell is enriched one level.

$$\Delta t \propto \frac{A/4}{s/2} = \frac{1}{2}\frac{A}{s} \tag{25}$$

For unsteady problems involving a pitching airfoil in forced harmonic motion, the effect of enrichment on the number of time-steps per cycle of motion can also be demonstrated. First the number of time-steps per cycle of motion N is related to the time-step by

$$N = \frac{\pi}{k M_\infty \Delta t} \tag{26}$$

where k is the reduced frequency and M_∞ is the freestream Mach number (since Δt is nondimensionalized by the freestream speed of sound). Therefore, the number of time-steps per cycle of motion is inversely related to the time-step.

$$N \propto \frac{1}{\Delta t} \tag{27}$$

Since the time-step is halved as the mesh is enriched one level, the number of time-steps required per cycle of motion doubles for a similar level of temporal convergence. Hence, the relationship between the number of time-steps per cycle of motion N required on a mesh to the number of time-steps per cycle of motion N_n on the same mesh using n levels of mesh enrichment can be stated as

$$N_n \approx 2^n N \tag{28}$$

As an example, suppose an unsteady problem on a coarse mesh requires 1250 time-steps per cycle of motion for a temporally converged solution. The same mesh and case using three levels of enrichment would require approximately 10000 time-steps per cycle of motion.

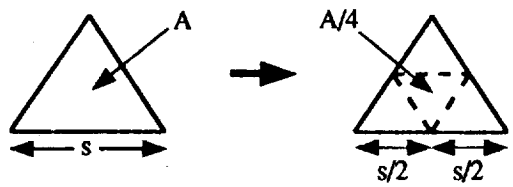

Fig. 5 Diagram illustrating change in characteristic length and area of an enriched computational cell.

Results and Discussion

Calculations were performed for the NACA 0012 airfoil to assess the accuracy and efficiency of the spatial adaption procedures. Steady and unsteady airfoil results are presented for comparison with published solutions using alternative methods and experimental data to determine the accuracy of the results. Timing comparisons are also made between results obtained using globally (estimated) and locally adapted meshes to determine the computational savings obtained by using the spatial adaption procedures.

Steady Results

Steady flow results were obtained for the NACA 0012 airfoil for comparison with results reported by Pulliam and Barton[20] and several other alternative methods for an inviscid case chosen by the AGARD Working Group 07, a subpanel of the AGARD Fluid Dynamics Panel. The case of

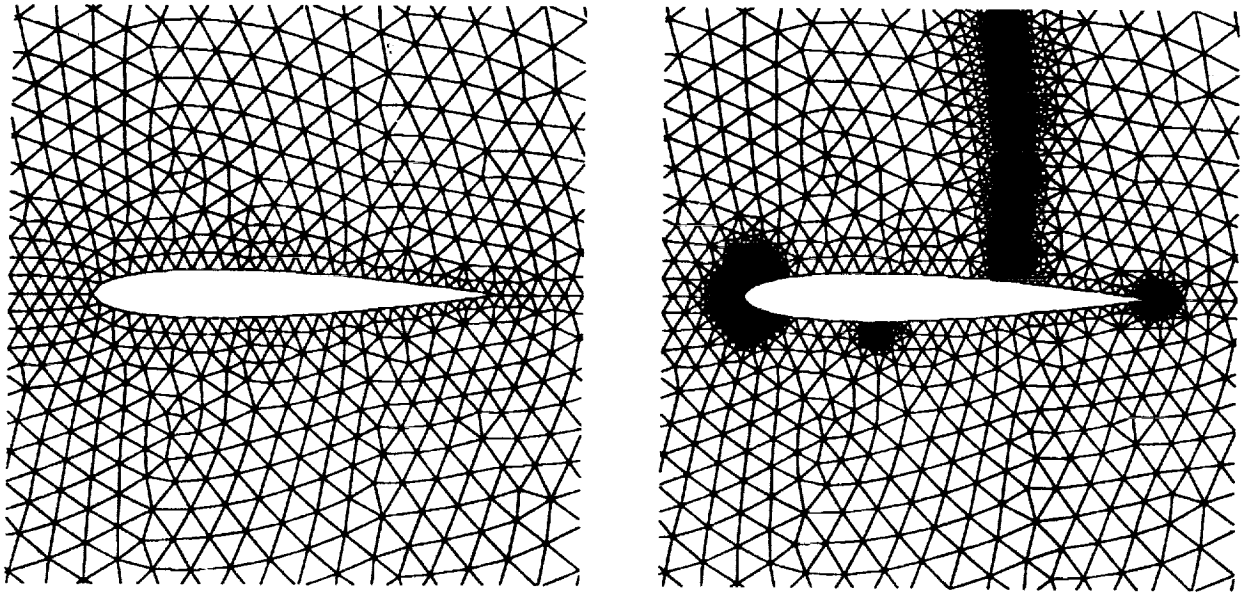

(a) original mesh. (b) adapted mesh.

Fig. 6 Comparison of meshes used in the calculation for the NACA 0012 airfoil at M_∞ = 0.8 and α_0 = 1.25°.

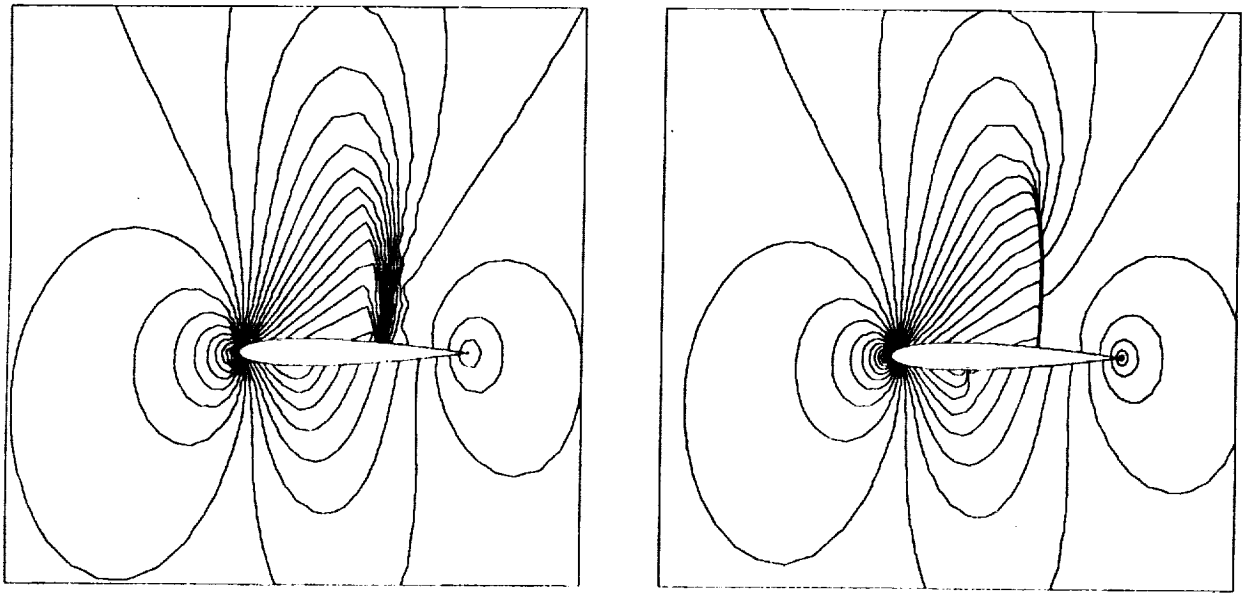

(a) original mesh. (b) adapted mesh.

Fig. 7 Comparison of pressure contour lines ($\Delta p = 0.025$) from solutions obtained for the NACA 0012 airfoil at M_∞ = 0.8 and α_0 = 1.25°.

interest is AGARD01, a NACA 0012 airfoil at a freestream Mach number of M_∞ = 0.8 and an angle of attack of α_0 = 1.25°. For this case, the starting mesh and final spatially adapted mesh are presented along with corresponding pressure contours for comparison with results of Ref. 20. The starting coarse mesh for the calculation, shown in Fig. 6(a), contains 1854 nodes and 3628 cells and extends 20 chordlengths to a circular outer boundary. The solution was obtained by adapting the mesh to the solution every 500 iterations for the first 2000 iterations (four levels of enrichment), and then the solution was converged to machine zero on the final adapted mesh. The final mesh after four levels of enrichment, shown in Fig. 6(b), contains 8947 nodes and 17653 cells. A comparison of pressure contours ($\Delta p = 0.025$) from the solutions obtained on the original mesh and the adapted mesh are shown in Figs. 7(a) and 7(b), respectively. For this case, there is a relatively strong shock wave on the upper surface of the airfoil near 62% chord and a relatively weak shock wave on the lower surface near 30% chord. The comparison between the two sets

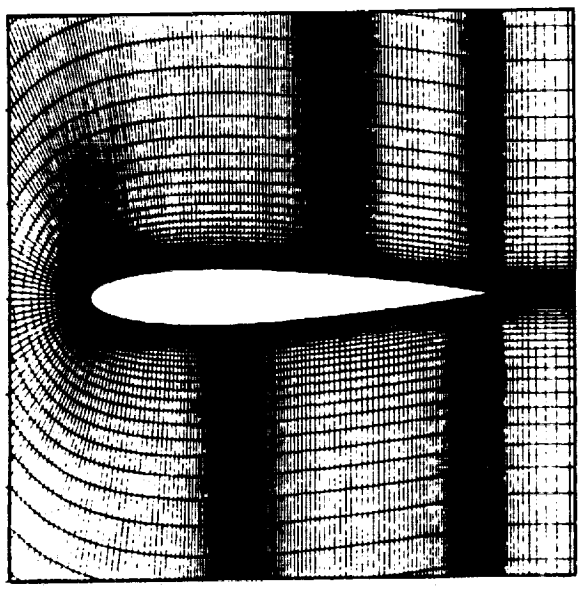

(a) mesh.

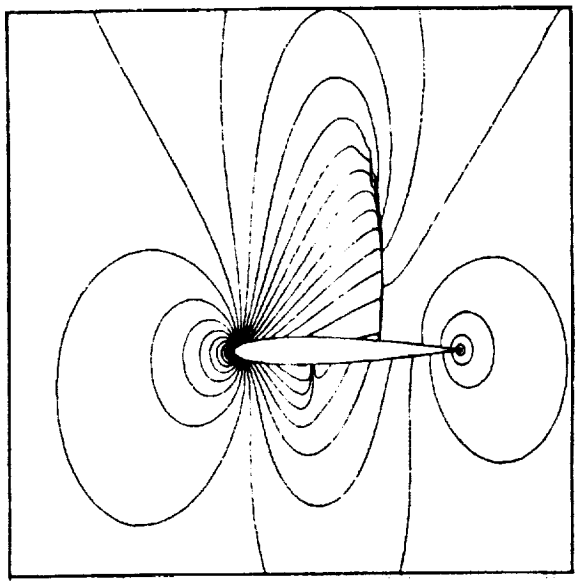

(b) pressure contours.

Fig. 8 Results from Pulliam and Barton[20] for the NACA 0012 airfoil at M_∞ = 0.8 and α_0 = 1.25°.

of contour lines reveals a considerable improvement in the shock resolution when spatial adaption is used. For further comparison, the mesh and pressure contour lines from the solution of Ref. 20 are shown in Fig. 8, which is believed to be one of the most accurate of the results generated by the alternative methods. Results from Ref. 20 were computed on a structured mesh of C-type topology containing 560 x 65 mesh points as shown in Fig. 8(a). This mesh indicates that points were clustered above and below the airfoil in the shock regions to produce a more accurate result. A comparison of the pressure contour lines from Pulliam and Barton,[20] shown in Fig. 8(b), with the contour lines shown in Fig. 7(b), obtained with the present spatial adaption procedure, indicates excellent agreement which verifies the accuracy of the adaption procedures. Finally, comparisons of computed lift, drag, and moment coefficients from the structured mesh solutions reported in Ref. 20 and the present results are given in Table 1. The present results are shown at the bottom of Table 1 and the coefficients listed from solutions 5 and 5* are from Pulliam and Barton.[20] The remaining solutions are from alternative methods and are included for completeness. Solution 5* is an improved result in comparison with solution 5, where improved boundary conditions and a finer mesh were used. A comparison of coefficients from the present solution with those of solution 5*, indicates agreement to within 1% for the lift and drag coefficients and to within 5% for the moment coefficient.

The computational savings for the steady flow problem can be estimated by comparing the number of cells in the adapted mesh to the number of cells in a globally fine mesh. The total number of cells for the globally fine mesh is computed by multiplying the number of cells in the starting coarse mesh by four (since each cell is divided into four smaller cells) raised to a power represented by the number of enrichment levels. Therefore, a globally fine mesh would contain 928768 cells (3628×4^1), which in comparison with the final adapted mesh containing 17653 cells, results in a computational savings of approximately fifty-three. If timing comparisons are made with solutions obtained using structured grid algorithms, the computational overhead of the indirect addressing of the unstructured grid algorithm must be accounted for. For example, the computational work for steady-state solutions obtained using unstructured grid algorithms have been shown to be 2 to 5 times more expensive than those obtained using structured

Table 1 Comparisons of computed lift, drag, and moment coefficients from the structured mesh solutions reported in Ref. 20 and the present results obtained using spatial adaption for the NACA 0012 airfoil at M_∞ = 0.8 and α_0 = 1.25°.

Soln#	Type	Mesh Size	c_l	c_d	c_m
1	C	189 X 25	0.3642	0.0225	-0.0376
2	C	188 X 24	0.3736	0.0244	-0.0411
3	O	158 X 23	0.3463	0.0223	-0.0358
5	C	249 X 67	0.3661	0.0229	-0.0430
6	O	192 X 39	0.3474	0.0221	-0.0374
8	O	128 X 28	0.3500	0.0221	-0.0370
9	O	320 X 64	0.3632	0.0230	-0.0397
5*	C	560 X 65	0.3618	0.0236	-0.0411
present	U	8947N, 17653C	0.3600	0.0238	-0.0390

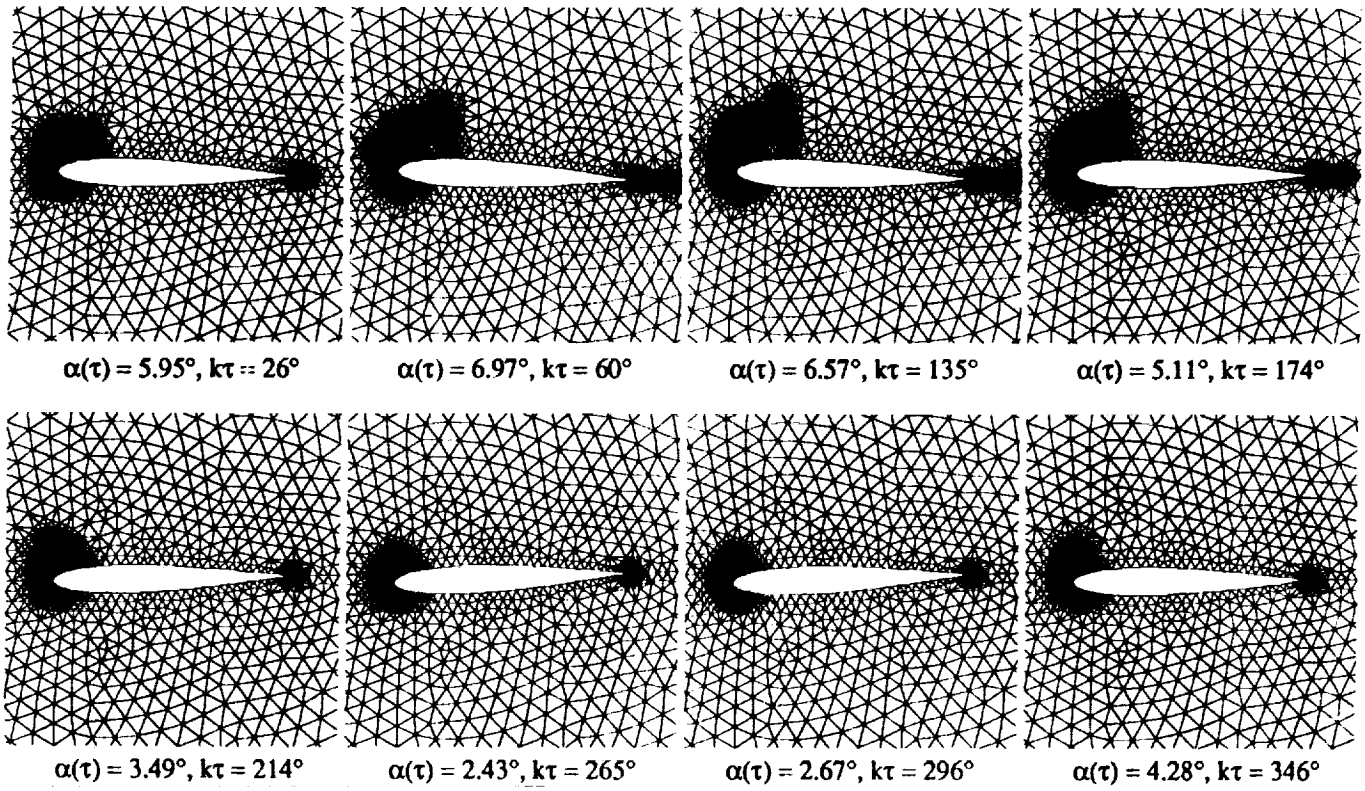

Fig. 9 Instantaneous meshes produced by the spatial adaption procedure for the NACA 0012 airfoil pitching harmonically at M_∞ = 0.599, α_0 = 4.86°, α_1 = 2.44°, and k = 0.0814.

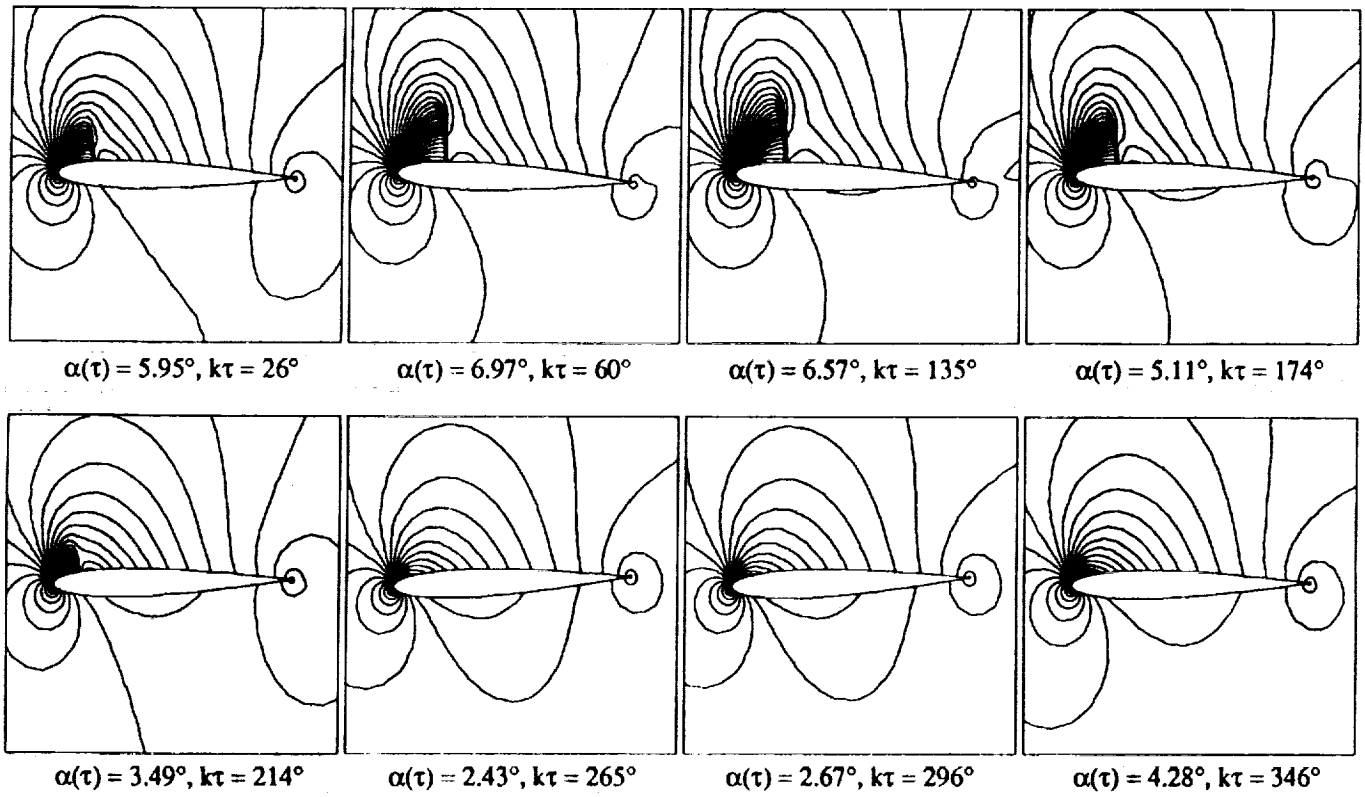

Fig. 10 Instantaneous contour lines ($\Delta\rho = 0.02$) from the spatially adapted solution for the NACA 0012 airfoil pitching harmonically at M_∞ = 0.599, α_0 = 4.86°, α_1 = 2.44°, and k = 0.0814.

grid algorithms.[21] Nonetheless, when spatial adaption procedures are used with unstructured grid algorithms, an order of magnitude computational savings can be achieved over solutions obtained using structured grid algorithms for comparable spatial accuracy.

Unsteady Results

Unsteady results are presented for the NACA 0012 airfoil using spatial adaption for AGARD cases 3 and 5, proposed by the AGARD Structures and Materials Panel.[22] Both cases involve the NACA 0012 airfoil pitching harmonically about the quarter chord at a reduced frequency based on semichord of k = 0.0814. The calculations were performed for three cycles of motion to obtain a periodic solution using 10000 time-steps per cycle starting with the same coarse mesh (Fig. 6(a)) that was used for the non-adapted steady flow result. During the course of the calculation, the mesh was spatially adapted every 10 time-steps using three levels of enrichment.

AGARD Case 3

Results were obtained for the airfoil pitching with an amplitude of α_1 = 2.44° at M_∞ = 0.599 and α_0 = 4.86° (referred to as AGARD case 3). Figure 9 shows the instantaneous adapted meshes and Fig. 10 shows the corresponding instantaneous density contour lines ($\Delta\rho$ = 0.02). The instantaneous meshes and density contour lines during the third cycle of motion were plotted at eight points in time. In each plot, the instantaneous pitch angle $\alpha(\tau)$ and the instantaneous angular position in the cycle $k\tau$ are noted. The instantaneous meshes (Fig. 9) clearly indicate the enrichment in regions near the shock wave on the upper surface of the airfoil and near the stagnation points. Figure 9 also shows that regions of the mesh near the moving shock and in the wake of the airfoil have been enriched and then coarsened throughout the cycle of motion. Specifically, the instantaneous mesh in Fig. 9 at $k\tau$ = 26° shows that the enrichment indicator works well for detecting the developing shock wave on the upper surface as is further shown in the density contours (Fig. 10). These density contours during the cycle demonstrate the ability of the spatial adaption procedures to produce sharp transient shock waves. The corresponding surface pressure distributions during the third cycle of motion are shown in Fig. 11 for comparison with the experimental data of Ref. 23. In each pressure plot the instantaneous pitch angle $\alpha(\tau)$ and the angular position $k\tau$ in the cycle are noted. During the first half of the cycle, there is a shock wave on the upper surface of the airfoil while the flow over the lower surface remains subcritical throughout the entire cycle. The pressure distributions indicate that the shock position oscillates over approximately 12% of the chord along the upper surface, requiring the spatial adaption procedure to track the movement and de-

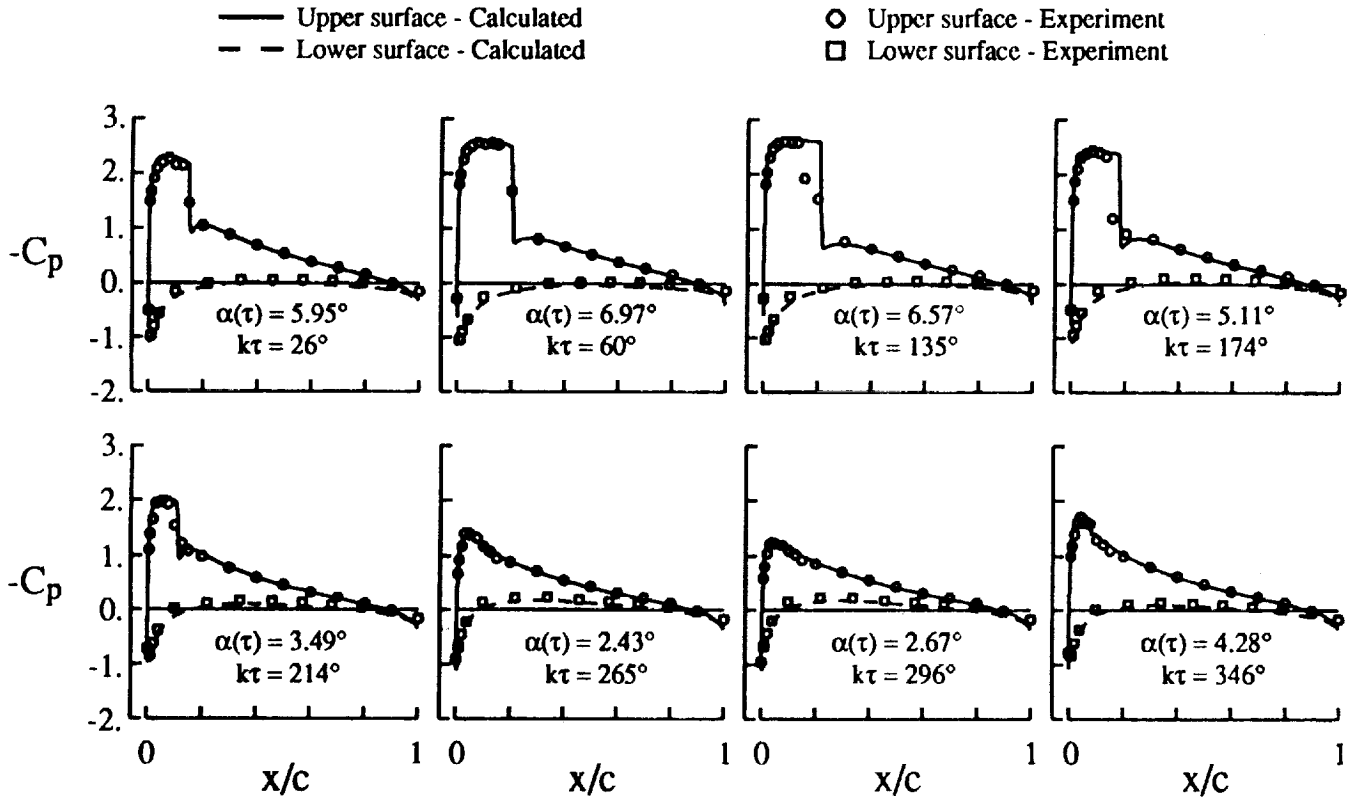

Fig. 11 Comparison of instantaneous pressure distributions for the NACA 0012 airfoil pitching harmonically at M_∞ = 0.599, α_0 = 4.86°, α_1 = 2.44°, and k = 0.0814 computed using spatial adaption.

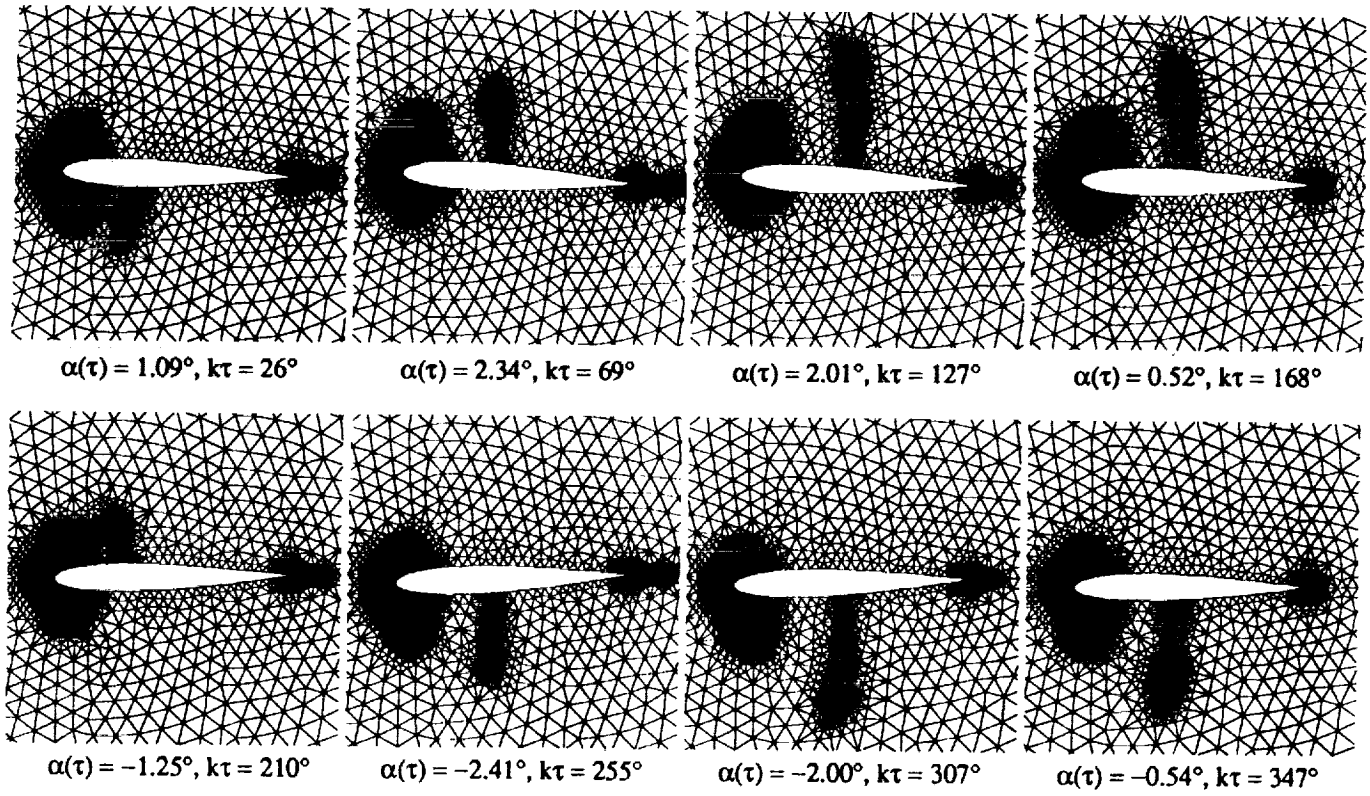

Fig. 12 Instantaneous meshes produced by the spatial adaption procedure for the NACA 0012 airfoil pitching harmonically at $M_\infty = 0.755$, $\alpha_0 = 0.016°$, $\alpha_1 = 2.51°$, and k = 0.0814.

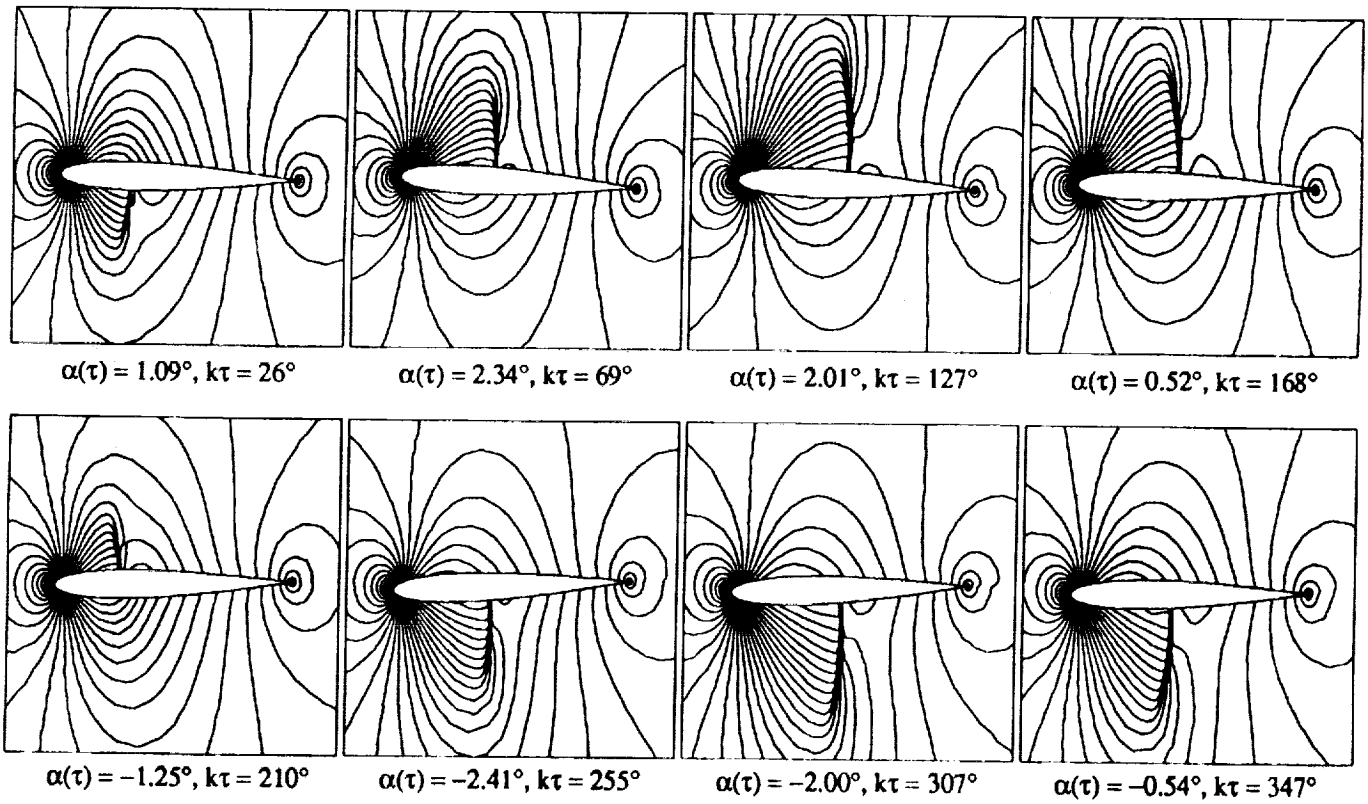

Fig. 13 Instantaneous contour lines ($\Delta\rho = 0.02$) from the spatially adapted solution for the NACA 0012 airfoil pitching harmonically at $M_\infty = 0.755$, $\alpha_0 = 0.016°$, $\alpha_1 = 2.51°$, and k = 0.0814.

velopment of the transient shock wave as it appears and disappears during the cycle. In general, the calculated results using the spatial adaption procedures compare well with the experimental data.

The computational savings obtained by using the spatial adaption procedures can be estimated by comparing the total number of cells marched in time with the estimated number of cells marched in time if a globally fine mesh were used. The total number of cells marched in time for the globally fine mesh is computed by multiplying the number of cells in the starting coarse mesh by the number of cycles, the number of time-steps per cycle, and four raised to the number of enrichment levels (since each cell is divided into four smaller cells). Therefore, for AGARD case 3, a total of 276 million cells were marched compared to 6966 million ($3628 \times 3 \times 10000 \times 4^3$) cells if a globally fine mesh were used, resulting in a computational savings of a factor of twenty-five. This factor does not include the computational overhead of the spatial adaption procedure, however, which was approximately 7% of the total CPU time.

AGARD Case 5

Results were obtained for the airfoil pitching with an amplitude of $\alpha_1 = 2.51°$ at $M_\infty = 0.755$ and $\alpha_0 = 0.016°$ (referred to as AGARD case 5). Figure 12 shows the instantaneous adapted meshes and Fig. 13 shows the corresponding instantaneous density contour lines ($\Delta\rho = 0.02$). The instantaneous meshes and density contour lines during the third cycle of motion were plotted at eight points in time. In each plot, the instantaneous pitch angle $\alpha(\tau)$ and the instantaneous angular position $k\tau$ in the cycle are noted. The instantaneous meshes (Fig. 12) clearly indicate the enrichment in regions near the shock waves and near the stagnation points. They also show coarsened regions where previously enriched regions have relatively small flow gradients. The density contours during the cycle (Fig. 13) demonstrate the ability of the spatial adaption procedures to produce sharp transient shock waves. The corresponding surface pressure distributions during the third cycle of motion are shown in Fig. 14 for comparison with experimental data.[23] In each pressure plot the instantaneous pitch angle $\alpha(\tau)$ and the angular position $k\tau$ in the cycle are noted. During the first part of the cycle there is a shock wave on the upper surface of the airfoil, and the flow over the lower surface is predominately subcritical. During the latter part of the cycle the flow about the upper surface is subcritical while a shock forms along the lower surface. The pressure distributions indicate that the shock position oscillates over approximately 25% of the chord along the upper and lower surfaces, requiring the spatial adaption procedure to accurately track the movement and development of the transient shocks. In general the calculated results using the spatial adaption procedures compare well with the experimental data. Figure 15 shows

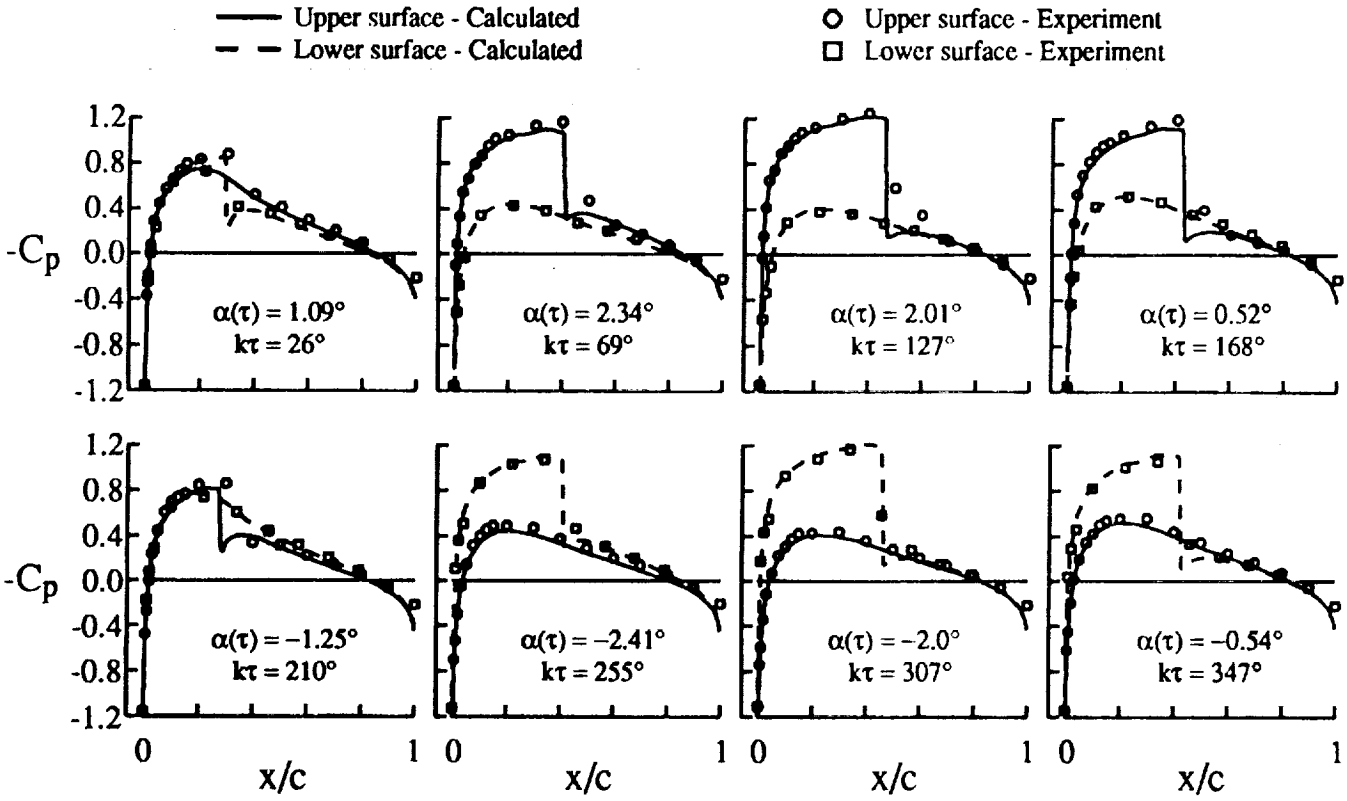

Fig. 14 Comparison of instantaneous pressure distributions for the NACA 0012 airfoil pitching harmonically at $M_\infty = 0.755$, $\alpha_0 = 0.016°$, $\alpha_1 = 2.51°$, and k = 0.0814 computed using spatial adaption.

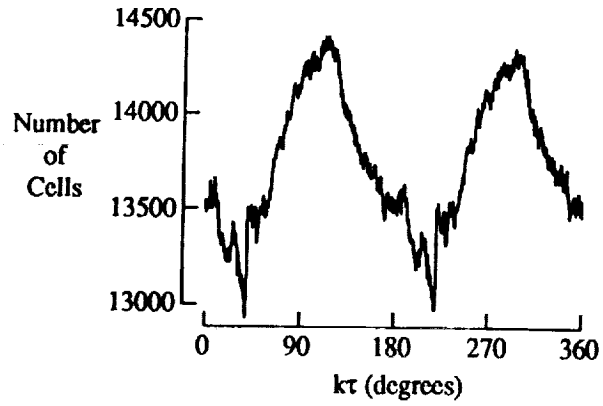

Fig. 15 Variation of number of cells throughout a cycle of motion for the NACA 0012 airfoil pitching harmonically at $M_\infty = 0.755$, $\alpha_0 = 0.016°$, $\alpha_1 = 2.51°$, and k = 0.0814.

the variation of the number of cells in the mesh throughout the third cycle of motion. In this figure, the maximum number of cells is approximately 14400 and the minimum number of cells is near 12900. These values indicate a significant computational savings when spatial adaption is used when compared to using a globally fine mesh of 232192 cells (comparable mesh density of 3 levels of enrichment on starting coarse mesh of 3628 cells is $3628 \times 4^3 = 232192$ cells) for similar spatial accuracy.

The computational savings obtained by using the spatial adaption procedures can again be estimated by comparing the total number of cells marched in time with the number of cells marched in time if a globally fine mesh were used. For AGARD case 5, a total of 413 million cells were marched compared to 6966 million cells for the globally fine mesh resulting in a computational savings of a factor of 17. This factor shows a decrease in savings compared to the savings factor obtained for AGARD case 3 due to the presence of a shock wave during the majority of the cycle of motion. Further, the computational savings factor does not include the computational overhead of the spatial adaption procedure which was approximately 7.5% of the total CPU time.

Concluding Remarks

Spatial adaption procedures for the accurate and efficient solution of steady and unsteady inviscid flow problems were described. The adaption procedures were developed and implemented within a two-dimensional unstructured-grid upwind-type Euler code. These procedures involve mesh enrichment and mesh coarsening to either add points in high gradient regions of the flow or remove points where they are not needed, respectively, to produce solutions of high spatial accuracy at minimal computational cost. A novel approach for detecting flow features based on the substantial derivative of density was used as an enrichment indicator. This enrichment indicator worked well for detecting developing shock waves in unsteady flows. This is a significant improvement over the more commonly used enrichment indicators based on the instantaneous solution (such as first or second differences in density) that miss the initial shock wave formation, especially for cases where the shock waves periodically appear and disappear in time.

Steady and unsteady transonic results were presented for the NACA 0012 airfoil to demonstrate applications of the spatial adaption procedures to two-dimensional problems. The unsteady flow results were obtained for an airfoil pitching harmonically about the quarter chord. Both the steady and unsteady solutions obtained using spatial adaption were shown to be of high spatial accuracy, primarily in that the shock waves were very sharply captured. Comparing the cost of results obtained on a spatially adapted mesh with the estimated cost of results obtained on a globally fine mesh of comparable mesh density, a computational savings of a factor of approximately fifty-three was achieved for the steady calculations using four levels of enrichment. Similar calculations using structured grid algorithms were estimated to be an order of magnitude more expensive for comparable spatial accuracy. Comparisons of coefficients from the spatial adaption solution with those of Pulliam and Barton,[20] indicated agreement to within 1% of the lift and drag coefficients and to within 5% for the moment coefficient. Similarly, for the unsteady calculations, a computational savings of a factor of as much as twenty-five was achieved and comparisons that were made with experimental pressure data indicated good agreement.

Acknowledgments

The work constitutes a part of the first author's Ph.D. thesis at Purdue University and was supported by the NASA Graduate Student Researchers program under grant NGT-50406. Also, the authors acknowledge Ken Morgan and Jaime Peraire of the Imperial College of Science, Technology, and Medicine, London, England for providing the grid generation program that was used to generate the grid for the NACA 0012 airfoil used in the present study.

References

[1] Thompson, J. F.; A Survey of Dynamically-Adaptive Grids in the Numerical Solution of Partial Differential Equations, AIAA Paper No. 84-1606, June 1984.

[2] Nakahashi, K.; and Deiwert, G. S.: Self-Adaptive-Grid Method with Application to Airfoil Flow, *AIAA Journal*, Vol. 25, No. 4, 1987, pp. 513-520.

[3] Usab, W. J.; and Murman, E. M.: Embedded Mesh Solution of the Euler Equation Using a Multiple-Grid Method, AIAA Paper No. 83-1946-CP, July 1983.

[4] Dannenhoffer, J. F.; and Baron, J. R.: Grid Adaption for the 2-D Euler Equations, AIAA Paper No. 85-0484, January 1985.

[5] Dannenhoffer, J. F.; and Baron, J. R.: Robust Grid Adaption for Complex Transonic Flows, AIAA Paper No. 86-0495, January 1986.

[6] Peraire, J.; Vahdati, M.; Morgan, K.; and Zienkiewicz, O. C.: Adaptive Remeshing for Compressible Flow Computations, *Journal of Computational Physics*, Vol. 72, pp. 449-466.

[7] Peraire, J.; Morgan, K.; Peiro, J.; and Zienkiewicz, O. C.: An Adaptive Finite Element Method for High Speed Flows, AIAA Paper No. 87-0558, January 1987.

[8] Lohner, R.; and Morgan, K.: Improved Adaptive Refinement Strategies for Finite Element Aerodynamic Computations, AIAA Paper No. 86-0499, January 1986.

[9] Lohner, R.; and Laboratory for Computational Physics and Fluid Dynamics: The Efficient Simulation of Strongly Unsteady Flows by the Finite Element Method, AIAA Paper No. 87-0555, January 1987.

[10] Lohner, R.: An Adaptive Finite Element Solver for Transient Problems with Moving Bodies, *Computers & Structures*, Vol. 30, pp. 303-317, 1988.

[11] Baum, J. D.; and Lohner, R.: Numerical Simulation of Shock-Elevated Box Interaction Using an Adaptive Finite-Element Shock Capturing Scheme, AIAA Paper No. 89-0653, January 1989.

[12] Lohner, R.: Adaptive H-Refinement on 3-D Unstructured Grids for Transient Problems, AIAA Paper No. 89-0365, January 1989.

[13] Lohner, R.; and Baum, J. D.: Numerical Simulation of Shock Interaction with Complex Geometry Three-Dimensional Structures Using a New Adaptive H-Refinement Scheme on Unstructured Grids, AIAA Paper No. 90-0700, January 1990.

[14] Rausch, R. D.; Batina, J. T.; and Yang, T. Y.: Euler Flutter Analysis of Airfoils Using Unstructured Dynamic Meshes, *Journal of Aircraft*, Vol. 27, No. 5, 1990, pp. 436-443.

[15] Batina, J. T.: Implicit Flux-Split Euler Schemes for Unsteady Aerodynamic Analysis Involving Unstructured Dynamic Meshes, AIAA Paper No. 90-0936, April 1990.

[16] Batina, J. T.: Accuracy of an Unstructured-Grid Upwind-Euler Algorithm for the ONERA M6 Wing, presented at the Accuracy of Unstructured Grid Techniques Workshop, NASA Langley Research Center, Hampton, Virginia, January 16-17, 1990.

[17] Batina, J. T.: Three-Dimensional Flux-Split Euler Schemes Involving Unstructured Dynamic Meshes, AIAA Paper No. 90-1649, June 1990.

[18] Van Leer, B.: Flux-Vector Splitting for the Euler Equations, *Lecture Notes in Physics*, Vol. 170, 1982, pp. 507-512.

[19] Holmes, D. G.; and Connell, S. D.: Solution of the 2D Navier-Stokes Equations on Unstructured Adaptive Grids, AIAA Paper No. 89-1392, June 1989.

[20] Pulliam, T. H.; and Barton, J. T.: Euler Computations of AGARD Working Group Test Cases, AIAA Paper No. 85-0018, January 1985.

[21] Proceedings: Accuracy of Unstructured Grid Techniques Workshop, NASA Langley Research Center, Hampton, Virginia, January 17-18, 1990.

[22] Bland, S. R., (compiler): *AGARD Two-Dimensional Aeroelastic Configurations*, AGARD-AR-156, August 1979.

[23] Landon, R. H.: NACA 0012. Oscillating and Transient Pitching, Data Set 3 in AGARD-R-702, Compendium of Unsteady Aerodynamic Measurements, August 1982.

NASA
National Aeronautics and Space Administration

Report Documentation Page

1. Report No.	2. Government Accession No.	3. Recipient's Catalog No.
NASA TM-104039		

4. Title and Subtitle

Spatial Adaption Procedures on Unstructured Meshes for Accurate Unsteady Aerodynamic Flow Computation

5. Report Date

March 1991

6. Performing Organization Code

7. Author(s)

Russ D. Rausch*, John T. Batina, and Henry T. Y. Yang*

*Purdue University, West Lafayette, IN 47907

8. Performing Organization Report No.

10. Work Unit No.

505-63-50-12

9. Performing Organization Name and Address

NASA Langley Research Center
Hampton, Virginia 23665-5225

11. Contract or Grant No.

13. Type of Report and Period Covered

Technical Memorandum

12. Sponsoring Agency Name and Address

National Aeronautics and Space Administration
Washington, DC 20546

14. Sponsoring Agency Code

15. Supplementary Notes

Presented as AIAA Paper No. 91-1106 at the AIAA/ASME/ASCE/AHS/ASC 32nd Structures, Structural Dynamics, and Materials Conference, Baltimore, Maryland, April 8-10, 1991

16. Abstract

Spatial adaption procedures for the accurate and efficient solution of steady and unsteady inviscid flow problems are described. The adpation procedures were developed and implemented within a two-dimensional unstructured-grid upwind-type Euler code. These procedures involve mesh enrichment and mesh coarsening to either add points in high gradient regions of the flow or remove points where they are not needed, respectively, to produce solutions of high spatial accuracy at minimal computational cost. The paper gives a detailed description of the enrichment and coarsening procedures and presents comparisons with alternative results and experimental data to provide an assessment of the accuracy and efficiency of the capability. Steady and unsteady transonic results, obtained using spatial adaption for the NACA 0012 airfoil, are shown to be of high spatial accuracy, primarily in that the shock waves are very sharply captured. The results were obtained with a computational savings of a factor of approximately fifty-three for a steady case and as much as twenty-five for the unsteady cases.

17. Key Words (Suggested by Author(s))	18. Distribution Statement
Computational Fluid Dynamics Unsteady Aerodynamics Transonic Flow	Unclassified - Unlimited Subject Category - 02

19. Security Classif. (of this report)	20. Security Classif. (of this page)	21. No. of pages	22. Price
Unclassified	Unclassified	16	A03